GSA Data Repository 2019177

Klausen, T.G., Nyberg, B., and Helland-Hansen, W., 2019, The largest delta plain in Earth's history: Geology, https://doi.org/10.1130/G45507.1

Supplementary Materials:

Materials and methods

Backstripping and reconstruction of paleobathymetric relief. Paleobathymetric relief in front of the Early Carnian delta plain is seen in depositional strike-oriented seismic profiles (Figure DR1) as northwest dipping seismic reflectors below channelized deposits depicted on attribute maps in Fig. 2. Basinward dipping reflectors are conditioned to an upper datum which was flat-lying at a time shortly after deposition. The distance between the underlying Ladinian (242-237 Ma) L1 sequence and the delta top of the Early Carnian (237-232 Ma) C1 interval (Klausen et al., 2015) represents the relief from basin floor created during transgression of the L1 sequence. The seismic profile in Figure DR1 is tied to a proximal nearby well (7324/7-1S) which illustrate the time-depth relationship for the seismic data and the age constraints offered by palynological data defining discrete stratigraphic intervals. The trajectory of successive platform edges steadily rises as the delta progrades, indicating a steady creation of accommodation. This is corroborated by the lack of deep incision

associated with the channelized deposits that can be seen as discontinuous high-amplitude seismic reflectors within the Snadd Formation interval (Figure DR1).

The interval between the tops of the L1 and C1 sequences is decompacted, and the paleobathymetric relief represented by the Top L1 transgressive surface is backstripped by removing the weight of the decompacted strata (Klausen and Helland-Hansen, 2018). The lithological composition of the decompacted interval was determined with computer-processed interpretation (CPI) of gamma ray, neutron, density and resistivity logs calibrated to core-plug measurements of helium porosity from cored intervals within wells 7324/10-1 and 7321/8-1 (Figure DR2). These wells were located close to the seismic profile analysed for paleobathymetry (Fig. 2). The well used to tie the seismic in Fig. S1 (7324/7-1S) is not associated with core intervals that could be used to quality control the CPI log estimates. Porosity-sand-silt-shale ratios for the C1 interval within wells 7321/8-1 and 7324/10-1 is 3.7-8.5-33.3-54.5 and 11-25-11.65-52.35, respectively. Using these values, the backstripped relief of the Top L1 transgressive surface is ~400 m, constrained by the horizontal asymptotes of the sigmoidal regression curve fitted to points along the reconstructed Top L1 MFS (Figure DR3).

Constraints on the Triassic Boreal Delta outline. The Barents Sea basin comprise Upper Triassic strata across most of its extent (Fig. 1C). However, along the western and northern margin of the basin, the strata experienced post-depositional normal faults that offset it to depths where it is not resolvable in seismic or penetrated by wells. Because of these limitations in data, Faleide et al. (2008) restrict their interpretation of the westward extent for Triassic deposits to the Bjørnøyrenna fault complex (Figure DR3). On Bjørnøya there are however Triassic deposits in outcrop (Vigran et al., 2014), and although the upper part of the succession is eroded, it shows many similarities with time-equivalent outcrops on Spitsbergen and the system likely extended much farther west than the Bjørnøyrenna Fault Complex. This

is confirmed by recent exploration wells southwest of Bjørnøya (7317/9-1), which attest to the presence of Triassic strata along the western margin. We therefore regard it as likely that the faulted crustal blocks with sedimentary strata of unassigned age along the western margin of the present Barents Sea basin comprise Triassic strata (Figure DR4A).

Late Triassic fine-grained channelized deposits are observed in outcrops on eastern Greenland (Hamann et al., 2005), but provenance data from these outcrops are not yet in the public domain. The geomorphological character of the most distal deposits in TBO does however not indicate that the river systems stopped before reaching this far west (Fig. 2). Evidence for the westward continuation of the TBO delta systems is provided by provenance data from time-equivalent strata in the Canadian Sverdrup Basin (Omma, 2009), where detrital zircon age signatures are identical to those observed in the Barents Sea. Being positioned between these two areas, the offshore and onshore Late Triassic stratigraphy of eastern Greenland (Hamann et al., 2005) should therefore also be considered to represent the westward continuation of TBO (Figure DR4B). By excluding Late Triassic deposits in Eastern Greenland and the Sverdrup Basin from the outline mapped in the present study, the TBO delta extent estimates represents a minimum scenario.

Profiles (Fig. 4) and seismic cross section (Figure DR2) from the Barents Sea and offshore northeastern Greenland show that several post-depositional normal faults offset Triassic strata. Extension associated with these tectonic features serve to overestimate the areal extent of the Triassic strata. The degree of extension is however more than compensated by excluding Triassic strata offshore Greenland from the aerial estimates. In addition has compression of Triassic strata during the collision between Svalbard and Greenland (Faleide et al., 2008) partially counteracted the effect of extensional stretching by folding, tilting and reverse faulting the Triassic strata of western Spitsbergen, as evident in outcrops of vertically tilted Triassic strata in eastern Spitsbergen (Vigran et al., 2014).

Constraints for possible TBO catchments. Catchment areas for TBO deltas are constrained by the Uralides in the southeast, where an orogeny was actively building in the Permian with a northward extension in Novaya Zemlya. Novaya Zemlya was gradually becoming inverted during the Middle to Late Triassic, evolving from a sedimentary basin in the Early Triassic[15] to a fold and thrust belt in the Late Triassic (Klausen et al., 2015). The elevated area developing over the fold and thrust belt constrains the catchment to the east. The Paleo-Tanafjord similarly constrains TBO catchment in the west (Eide et al., 2017). Because different scenarios for the extent of this catchment has been calculated, TBO catchments have different westward extents.

Southward, TBO catchment extent is constrained by three possible scenarios. Our minimum catchment extent is constrained by the present Barents Sea drainage, including the northward flowing Dvina and Pechora rivers, an area of ~1.1 x 10^6 km^2. We also hypothesise a mid-range catchment estimate constrained by the present Volga drainage. This drainage basin is presently flowing southward to the Black Sea, but as part of the Uralian foreland it flowed northward in the Triassic[3] and could potentially have formed a watershed divide in the Triassic[28]. In this scenario, the catchment for TBO is ~3.3 x 10^6 km^2. Our preferred scenario however extends southward to the Variscan orogen, roughly corresponding to the southern limit of the Black Sea and the Caucasus Mountains (Golonka, 2007). This catchment scenario totals ~6.8 x 10^6 km^2.

Review of modern and LGM delta outlines. The largest modern deltas around the world are based on the delineations of Tessler et al. (2015). The LGM deltas were selected based on the distribution of modern deltas that could accommodate a large low-lying delta plain during a LGM low-stand. The along-dip extent of LGM deltas is defined from present-day shoreline to its continental shelf break based on global SRTM 30 Plus bathymetric data (Becker et al., 2009). The along-strike extent of the potential delta plain is constrained by bathymetric

drainage profiles that show catchment coalescence during a low-stand at present day continental shelf edge.

While we recognize that post-glacial retreat and continental shelf currents will influence the present-day bathymetry, the large-scale drainage profiles reflect the overall plate tectonic configurations and provide reasonable constraints for the potential extent of LGM delta plains. We include modern deltas in the LGM delta plain outline in order to avoid underestimating the maximum landward extent potentially posed by the fluvial equilibrium profiles and landward apices of LGM deltas overprinted by modern deltas (Blum et al., 2013). Our dataset excludes LGM estimates that were characteristic of grounded ice sheets during glaciations (Jakobsson et al., 2016). The area of modern and LGM deltas (Supplementary Table 1) are extracted in a Cylindrical Equal Area projection while LGM deltas in polar regions are visualized in Fig. 4B (Bering, East Siberian and Laptev Sea) by a Lambert azimuthal equal area projection.

Review of ancient delta outlines. We acknowledge that estimating outlines of ancient delta systems is a challenging task. Compilations of global paleogeographic maps will never be able to offer in-depth, accurate estimates of ancient delta outlines, but they offer a review of regions with large-scale terrestrial deposits through different times in Earth's history. We have adopted Jan Golonka's compilations of paleogeographic maps (Golonka, 2007), and have reviewed each of the largest possible deltaic areas shown in his compilations. Some areas of the world, such as for example the Permo-Triassic Tethyan Realm are depicted with widespread terrestrial deposits (Golonka, 2007), but on closer inspection these areas evidently comprise multiple systems that are mainly alluvial in nature and have relatively restricted deltaic depositional environments (e.g. the Minjur Formation on the Arabian peninsula [Alsharhan, 1993], or the terrestrial deposits of Central Europe [McKie and Williams, 2009]).

Such areas are omitted from the present comparison. Surface area of possible ancient deltas (Fig. 4) are given in Table 1.

Reconstructing the outline of the McMurray Formation is an example of typical difficulties when evaluating the outline of ancient deltas: the eastern limit of the formation has experienced post-depositional erosion (Sathiamurthy and Voris, 2006) in a similar manner as TBO in northern parts of Svalbard. The outline of the McMurray Formation used to compare to TBO is therefore extended a few kilometres eastward as an approximation that accounts for post-depositional erosion and is not under-estimating the possible full extent of the formation.

References cited in Supplementary Text

Alsharhan, A.S., 1993, Sedimentary facies analysis of the subsurface Triassic and hydrocarbon potential in the United Arab Emirates. Facies, 28, p. 97-108.

Becker, J.J., Sandwell, D.T., Smith, W.H.F., Braud, J., Binder, B., Depner, J., Fabre, D., Factor, J., Ingalls, S., Kim, S.H. and Ladner, R., 2009, Global bathymetry and elevation data at 30 arc seconds resolution: SRTM30_PLUS. Marine Geodesy, 32, p. 355-371.

Benyon, C., Leier, A., Leckie, D.A., Webb, A., Hubbard, S.M. and Gehrels, G., 2014, Provenance of the Cretaceous Athabasca Oil Sands, Canada: Implications for continental-scale sediment transport. Journal of Sedimentary Research, 84, p. 136-143.

Blum, M.D., Milliken, K.T., Pecha, M.A., Snedden, J.W., Frederick, B.C. and Galloway, W.E., 2017, Detrital-zircon records of Cenomanian, Paleocene, and Oligocene Gulf of Mexico drainage integration and sediment routing: Implications for scales of basin-floor fans. Geosphere, 13, p. 2169-2205.

Blum, M., Martin, J., Milliken, K. and Garvin, M., 2013, Paleovalley systems: insights from Quaternary analogs and experiments. Earth-Science Reviews, 116, p. 128-169.

Cassinis, G., Perotti, C.R. and Ronchi, A., 2012, Permian continental basins in the Southern Alps (Italy) and peri-mediterranean correlations. International Journal of Earth Sciences, 101, p. 129-157.

di Pasquo, M.M. and Grader, G.W., 2012, The palynology of the Lower Permian (Asselian-? Artinskian) Copacabana Formation of Apillapampa, Cochabamba, Bolivia. Palynology, 36, p. 264-276.

Dubiel, R.F., Hasiotis, S.T., Davidson, S.K., Leleu, S. and North, C.P., 2011, Deposystems, paleosols, and climatic variability in a continental system: the Upper Triassic Chinle Formation, Colorado Plateau, USA. From River to Rock Record: The Preservation of Fluvial Sediments and their Subsequent Interpretation: SEPM (Society for Sedimentary Geology) Special Publication, 97, p. 393-421.

Guiraud, R. and Bosworth, W., 1999, Phanerozoic geodynamic evolution of northeastern Africa and the northwestern Arabian platform. Tectonophysics, 315, p. 73-104.

Gouramanis, C. and McLoughlin, S., 2016, Siluro-Devonian trace fossils from the Mereenie Sandstone, Kings Canyon, Watarrka National Park, Amadeus Basin, Northern Territory, Australia. Alcheringa: An Australasian Journal of Palaeontology, 40, p. 118-128.

Hamann, N.E., Whittaker, R.C. and Stemmerik, L., 2005, Geological development of the Northeast Greenland shelf. *In:* Geological Society, London, Petroleum Geology Conference series, Vol. 6, No. 1, p. 887-902. Geological Society of London.

Helland-Hansen, W., Ashton, M., Lømo, L. and Steel, R., 1992, Advance and retreat of the Brent delta: recent contributions to the depositional model. Geological Society, London, Special Publications, 61, p. 109-127.

Jakobsson, M., Nilsson, J., Anderson, L., Backman, J., Björk, G., Cronin, T.M., Kirchner, N., Koshurnikov, A., Mayer, L., Noormets, R. and O'Regan, M., 2016, Evidence for an ice

shelf covering the central Arctic Ocean during the penultimate glaciation. Nature communications, 7, DOI: 10.1038/ncomms10365.

Klausen, T.G., Ryseth, A.E., Helland-Hansen, W., Gawthorpe, R. and Laursen, I., 2015, Regional development and sequence stratigraphy of the Middle to Late Triassic Snadd formation, Norwegian Barents Sea. Marine and Petroleum Geology, 62, p. 102-122.

McIlroy, D., Flint, S., Howell, J.A. and Timms, N., 2005, Sedimentology of the tide-dominated Jurassic Lajas Formation, Neuquén Basin, Argentina. Geological Society, London, Special Publications, 252, p. 83-107.

McKie, T. and Williams, B., 2009, Triassic palaeogeography and fluvial dispersal across the northwest European Basins. Geological Journal, 44, p. 711-741.

Omma, J.E., 2009, Provenance of Late Paleozoic and Mesozoic sediment to key Arctic basins: implications for the opening of the Arctic Ocean [Ph.D. thesis]: University of Cambridge, 235 p.

Pieñkowski, G., 2004, The epicontinental Lower Jurassic of Poland. Polish Geological Institute Special Papers, 12, p. 1-154.

Visser, J.N.J., 1987, The palaeogeography of part of southwestern Gondwana during the Permo-Carboniferous glaciation. Palaeogeography, Palaeoclimatology, Palaeoecology, 61, p. 205-219.

Supplementary Figure Captions

Figure DR1: Cross-sectional character of the delta system. Seismic cross section through the distal part of the delta plain showing the paleobathymetric relief and channelized deposits of the Early Carnian delta plain. Profile is flattened relative to the Top C1 MFS, which represents a paleo-horizontal datum to the basinward dipping reflectors below. Location of profile is shown in Fig. 2.

Figure DR2: Input data for backstripping paleobathymetry. CPI well logs of 7321/8-1 (distal) and 7324/10-1 (proximal) that are used as input for the lithology fraction in the decompaction and backstripping of the paleobathymetric relief. MD = Measured Depth (m); GR = Gamma Ray (API); ResD = Deep Resistivity (ohm); ResXO = Micro Resistivity (ohm); NEU = Neutron Porosity (m^3/m^3); DEN = Density (g/cm^3); Vclay = Clay Volume (%); Vsilt = Silt Volume (%); Vsand = Sand Volume (%); and Hpor = Helium Porosity (%, point measurements from core plugs).

Figure DR3: Numerically defined parameters define relief and gradient. Sigmoidal regression curve f(x) fitted to georeferenced points along the reconstructed surface of Top L1 MFS shown in Fig. S1. Derivative of the surface f'(x) show a maximum slope inclination of c. 1.47 degrees. F(x) is compared to modern continental shelves in Fig. 4D.

Figure DR4: Westward continuation of TBO beyond the present outline. Geoprofile of the conjugate margins of A) western Barents Sea and B) northeast Greenland, modified from Faleide et al. *(19)* and Hamann et al. *(17)* respectively. Black arrow in A) illustrate the westward extent of the minimum scenario for the TBO delta outline considered in the present study. The maximum regressive stage of the Early Carnian delta likely incorporates Triassic strata present within the Lower Mesozoic interval on northeastern Greenland.

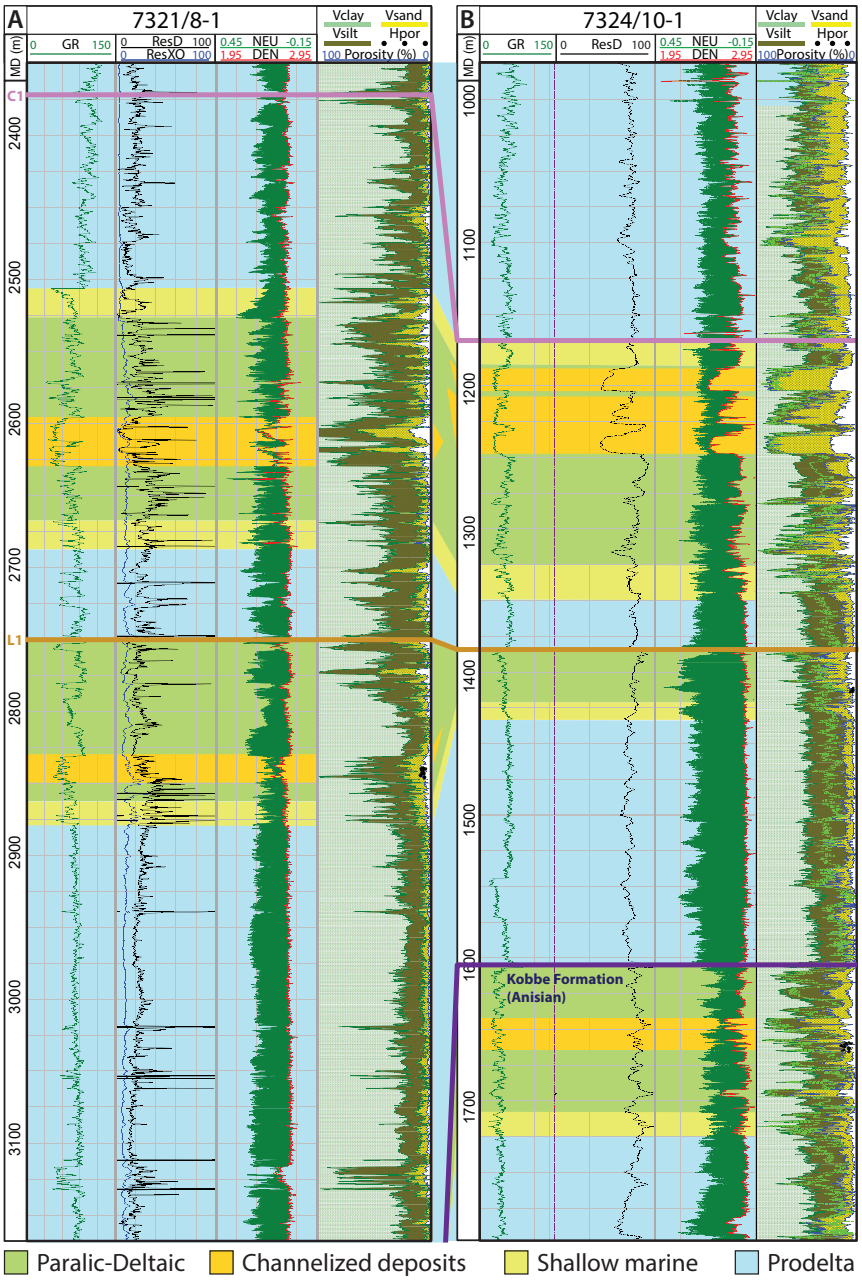
A
7321/8-1
B
7324/10-1
Vclay
Vsand
Vsilt
Hpor
GR
ResD
ResXO
NEU
DEN
Porosity (%)
MD (m)
C1
L1
Kobbe Formation
(Anisian)
Paralic-Deltaic
Channelized deposits
Shallow marine
Prodelta

Figure DR1

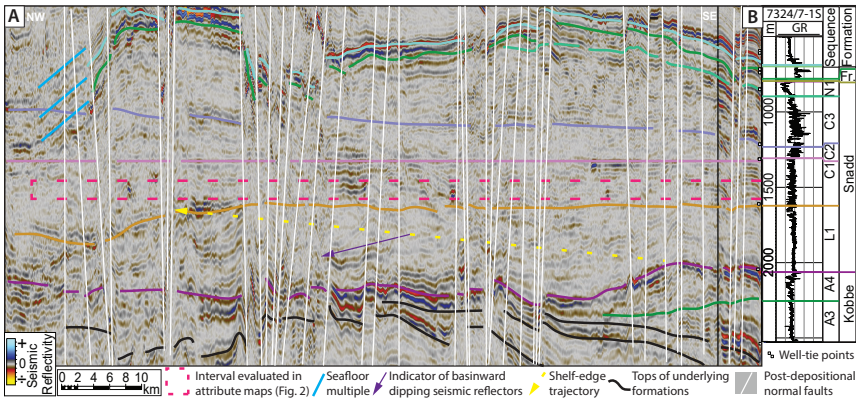
A
NW
SE
B
7324/7-1S
GR
Sequence
Formation
Fr.
N
C3
C2
C1
Snadd
L1
A4
A3
Kobbe
1000
1500
2000
Well-tie points
+
0
-
Seismic Reflectivity
0 2 4 6 8 10
km
Interval evaluated in attribute maps (Fig. 2)
Seafloor multiple
Indicator of basinward dipping seismic reflectors
Shelf-edge trajectory
Tops of underlying formations
Post-depositional normal faults

Figure DR2

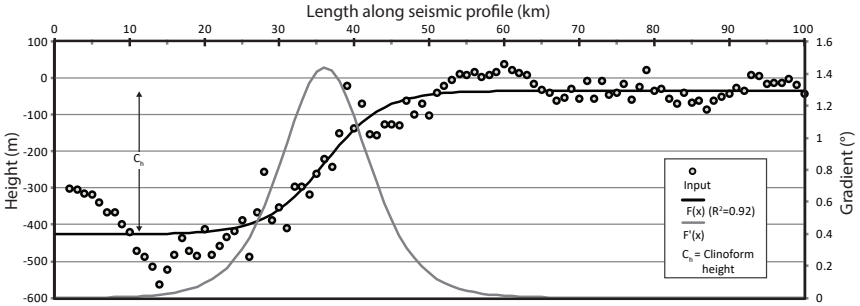
Length along seismic profile (km)
0
10
20
30
40
50
60
70
80
90
100
Height (m)
100
0
-100
-200
-300
-400
-500
-600
Gradient (°)
1.6
1.4
1.2
1
0.8
0.6
0.4
0.2
0
C_h
Input
F(x) (R^2=0.92)
F'(x)
C_h = Clinoform height

Figure DR3

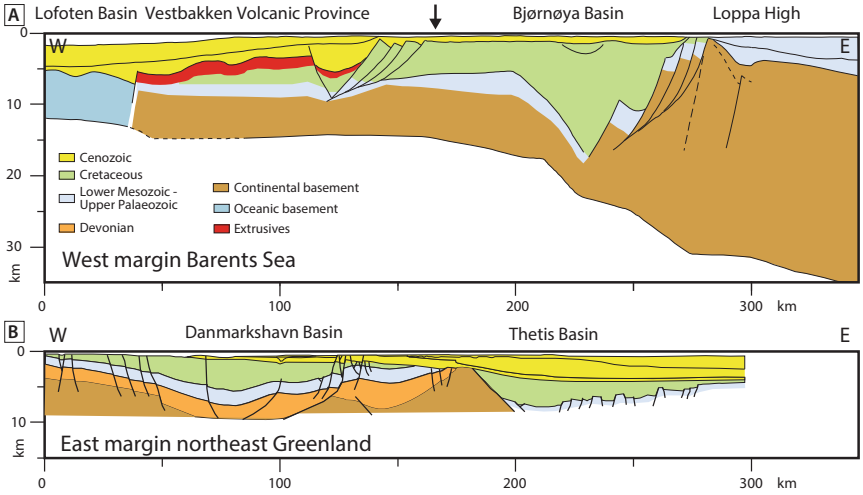
A
Lofoten Basin
Vestbakken Volcanic Province
Bjørnøya Basin
Loppa High
W
E
0
10
20
30
km
Cenozoic
Cretaceous
Lower Mesozoic - Upper Palaeozoic
Devonian
Continental basement
Oceanic basement
Extrusives
West margin Barents Sea
0
100
200
300
km
B
W
Danmarkshavn Basin
Thetis Basin
E
0
10
km
East margin northeast Greenland
0
100
200
300
km

Figure DR4

Table DR1. Summary of the largest modern, LGM and ancient delta plain areas. *Based on modern delta delineations of Tessler et al. (2015). † See Figure 4 of the main text for largest delta outlines. ‡ Defined as terrestrial deposits near the coast, not necessarily deltaic, in original reference (Golonka, 2007).

Modern Delta*†	Area (10^4 km^2)	LGM Delta†	Area (10^4 km^2)	Ancient Delta†	Area (10^4 km^2)
Amazon	10.8	Sunda Shelf	130	TBO	165
Ganges-Brahmaputra	9.20	Gulf of Carpentaria	90.1	McMurray (Benyon et al., 2014)	110
Mekong	5.04	Chukchi Sea	82.6	Kamienna Group (Pieñkowski, 2004)	71.4
Yangtze	3.67	Yellow Sea	81	Cretaceous Gulf of Mexico (Blum et al., 2017)	23.6
Irrawaddy	3.3	Bering Sea	80.9	Paleocene Gulf of Mexico (Blum et al., 2017)	20.2
Mississippi	2.90	East Siberia Sea	74	Brent Group (Helland-Hansen et al., 1992)	5.29
Nile	2.78	Laptev Sea	72.7	Neuquen Basin‡ (McIlroy et al., 2005)	134
Orinoco	2.67	North Sea	64.3	Chinle Formation‡ (Dubiel et al., 2011)	128
Chao Phraya	2.36	Java Sea	48.2	Titicaca Group‡ (di Pasquo and Grader, 2012)	127
Lena	2.03	Sea of Okhotsk	37.6	Dwyka Group‡ (Visser, 1987)	127
Niger	1.86	Baltic Sea	37.1	Val Gardena Sandstone‡ (Cassinis et al., 2012)	66.3
Rio Grande	1.58	Amazon	34.5	Saad/Aheimer Formations‡ (Guiraud and Bosworth, 1999)	65.4
Parana	1.52	Persian Gulf	25.2	Mereenie Sandstone‡ (Gouramanis and McLoughlin, 2016)	51.8